Radial distributions of equatorial phase space density for outer radiation belt electrons

D. L. Turner,[1] V. Angelopoulos,[1] Y. Shprits,[1,2] A. Kellerman,[1] P. Cruce,[1] and D. Larson[3]

Received 16 March 2012; revised 11 April 2012; accepted 12 April 2012; published 11 May 2012.

[1] We present the first direct observations of equatorial electron phase space density (PSD) as a function of the three adiabatic invariants throughout the outer radiation belt using data from the Solid State Telescopes on THEMIS-D. We estimate errors in PSD that result from data fitting and uncertainty in the calculation of the second and third invariants based on performance-weighted results from seven different magnetic field models. The PSD gradients beyond geosynchronous orbit (GEO) are energy dependent, revealing different source regions for the relativistic and non-relativistic populations. Specifically, the PSD distribution of outer belt relativistic electrons is peaked near L* ≈ 5.5. These features are typical for the outer belt, based on a survey of a two-month period from 01 Feb.–31 Mar. 2010. The results are consistent with previous studies, which were based on off-equatorial observations, but remove the high uncertainties introduced from mapping by using truly equatorial measurements (i.e., within only a few degrees of the magnetic equator) and quantifying the error in PSD. The newly calibrated THEMIS-SST dataset forms a powerful tool for exploration of the near-Earth magnetosphere, especially when combined with the upcoming RBSP mission. **Citation:** Turner, D. L., V. Angelopoulos, Y. Shprits, A. Kellerman, P. Cruce, and D. Larson (2012), Radial distributions of equatorial phase space density for outer radiation belt electrons, *Geophys. Res. Lett.*, *39*, L09101, doi:10.1029/2012GL051722.

1. Introduction

[2] Many outstanding questions remain considering the mechanisms responsible for source, loss, and transport of outer radiation belt electrons. To study these mechanisms, it is beneficial to examine electron observations in phase space density (PSD) as a function of the three adiabatic invariants, $f(\mu, K,$ and $L^*)$ (see definitions in *Green and Kivelson* [2004], and note, L^* is inversely proportional to the drift invariant, Φ), since Liouville's theorem states that in the absence of external sources or losses, PSD is conserved along trajectories in phase space. PSD can be converted from the standard, six-dimensional phase space, by assuming phase averaging over the three characteristic motions of particles trapped in Earth's magnetic field. These PSD distributions of outer radiation belt electrons are telltale of the source, loss, and transport mechanisms and, for this reason, have been the focus of many recent outer radiation belt studies. Here, we concentrate on how $f(\mu, K,$ and $L^*)$ can be used to study electron source and acceleration mechanisms.

[3] Using PSD as a function of μ, K, and L^* calculated from electron fluxes measured by the Polar spacecraft, *Selesnick and Blake* [2000] found peaks in PSD at L^* between 4 and 6 for μ = 200 and 800 MeV/G and K = 1.0 $G^{1/2}R_E$, which they concluded indicated a localized source of electrons within the heart of the outer belt. However, they discussed how the location in L^* of the peak and magnitude of PSD varied significantly when calculated for different magnetic field models. *Green and Kivelson* [2004] also calculated PSD as a function of μ, K, and L^* using Polar data. They also found peaks in the relativistic PSD profiles, but they discussed the uncertainties in the results due to model error when calculating K for the high latitude Polar observations. *Chen et al.* [2007] presented compelling evidence of local acceleration as a source of relativistic electrons using off-equatorial PSD distributions in L^* for fixed μ and K that revealed a peaked distribution with a radial profile time history that increased first around GEO and then later at higher and lower L^*. Recent results produced by data assimilation using CRRES data, a radial diffusion model, and a Kalman filter also reveal peaks in the relativistic electron PSD L^*-distributions [e.g., *Shprits et al.*, 2007]. *Chen et al.* [2005] and *Turner and Li* [2008] found that the PSD distributions of near-equatorial electrons were μ-dependent beyond geosynchronous orbit (GEO). The sign of the PSD gradients were often positive for the low-energy (<∼200 MeV/G) electrons but negative for those at higher energy, indicating different source regions for the two populations. *Kim et al.* [2010] conducted a similar study and found the μ-dependent results were consistent for off-equatorial electrons. However, none of these studies were able to show peaks in the equatorial population, which is important since local acceleration by chorus [e.g., *Summers et al.*, 1998; *Horne et al.*, 2005] should be most efficient for electrons with equatorial pitch angles near 90°. For a more detailed discussion of previous PSD studies, including several others not referenced here, see *Green and Kivelson* [2004] and/or *Turner et al.* [2010].

[4] Motivated by the recent availability of the THEMIS dataset near the magnetic equator, we seek to reexamine the radial PSD profiles of tens to hundreds MeV/G electrons from this ideal, near-equatorial vantage point. We calculate PSD as a function of the three adiabatic invariants for equatorially mirroring electrons (i.e., $K \approx 0$ $G^{1/2}R_E$) over a

[1]Department of Earth and Space Sciences, University of California, Los Angeles, California, USA.
[2]Department of Atmospheric and Oceanic Sciences, University of California, Los Angeles, California, USA.
[3]Space Sciences Laboratory, University of California, Berkeley, California, USA.

Corresponding author: D. L. Turner, Department of Earth and Space Sciences, University of California, Los Angeles, CA 90095-1567, USA. (drew.lawson.turner@gmail.com)

0094-8276/12/2012GL051722

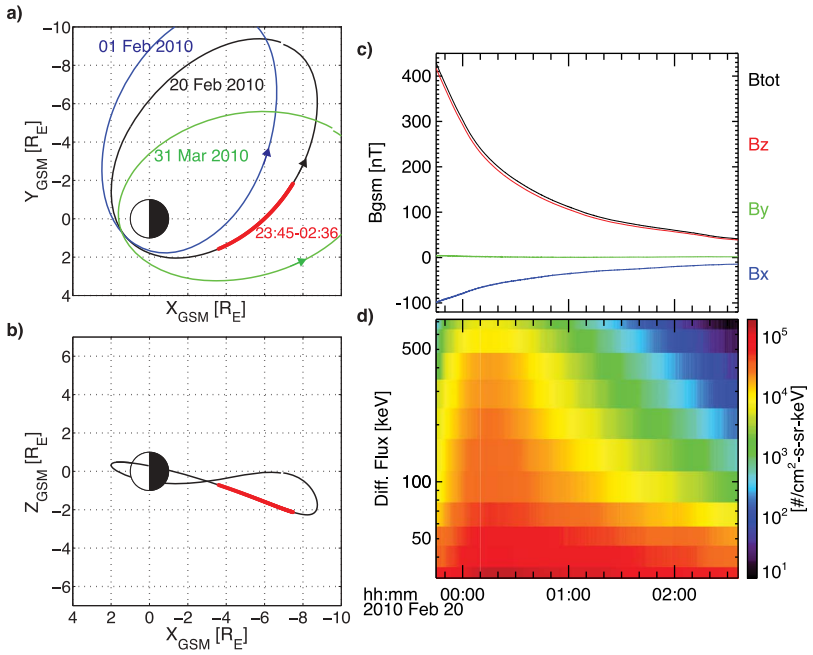

Figure 1. THEMIS-D orbits and magnetic field and flux data from the example period. (a) TH-D orbital projections in the XYgsm plane for 01 Feb. (blue), 20 Feb. (black), and 31 Mar. (green) of 2010. Arrows indicate the direction of travel on each orbit. The portion of the orbit on 20 Feb. 2010 indicated in red corresponds to the period (23:45–02:36 UT) examined in detail in this paper and the data shown in Figures 1c and 1d. (b) TH-D orbital projection in the XZgsm plane for 20 Feb. 2010, with the same period of interest shown in Figure 1a indicated in red. (c) TH-D FGM magnetic field strength (black) and components in GSM (X: blue, Y: green, Z: red) for 23:45–02:36 UT on 19–20 Feb. 2010. (d) TH-D SST electron differential fluxes shown in color for 11 of the instrument's differential energy channels ranging from ~30–700 keV.

broad range in energy, from 10's of keV to >1 MeV, and L^*, covering the entirety of the outer belt from the slot region into the plasma sheet. We also present details of a thorough error analysis that is used to account for uncertainty in PSD due to data fitting and error in K as well as uncertainty in L^* from imperfect magnetic field models. The following sections present the dataset used, the methodology to convert from flux to PSD with details of the error analysis, and the initial results of this study. We conclude with a brief discussion of the implications of these results as we enter a new era in radiation belt research with the upcoming launch of NASA's Radiation Belt Storm Probes (RBSP) mission.

2. Data

[5] NASA's Time History of Events and Macroscale Interactions during Substorms (THEMIS) mission [*Angelopoulos*, 2008], consisted of five identically instrumented spacecraft in highly elliptic orbits near the magnetic equatorial plane between 2007 and 2010. Since 2010, three spacecraft are still operational as part of the THEMIS mission: THEMIS-A (THA), THD, and THE. Of the different particles and fields instruments available, we employ magnetic field data from the fluxgate magnetometer (FGM) [*Auster et al.*, 2008] and energetic (i.e., E > ~30 keV) electron fluxes from the solid state telescopes (SSTs) on THD. For this study, we use data from THD only to avoid any ambiguity due to magnetic field mapping between different spacecraft.

[6] Each spin-stabilized THEMIS spacecraft carries four SST instruments, which provide full distribution functions of the energetic electron and ion populations from each 3-second spin. The SSTs consist of a core of three solid-state detectors, surrounded by aluminum shielding. Two apertures, one on each of the electron and ion sides of the instruments, allow particle access to both sides of the detector stack. The electron side uses a thin foil to absorb contaminating protons below ~350 keV. On the ion side, contaminating electrons below ~300 keV are swept away using a permanent magnet. The shared middle detector is used for coincidence logic for higher energy electrons (E > ~350 keV) and protons (E > ~6.5 MeV). Recently, SST performance was characterized using Geant4 simulations, and the resulting response functions have been applied to the data, producing a much more consistent dataset when compared with corresponding data from the lower-energy electrostatic analyzers (ESAs) [*McFadden et al.*, 2008]. Geant4 was also used to characterize sources of signal contamination, such as cross-contamination from other particle species and shield-penetrating electrons. Additionally, the four SSTs on each spacecraft have recently been intercalibrated, providing accurate angular distributions.

[7] For this study, we use THD magnetic field and flux data to derive outer belt electron PSD for constant μ and K over the period 01 February–31 March 2010. Figure 1a shows the THD orbits in the XY-GSM plane for the start and end days of this period. We chose this period because THD was in fast survey mode during the outbound portions of its orbits, and these outbound trajectories traversed the outer radiation belt in the midnight magnetic local time (MLT) sector. For each day in this period, we calculated electron PSD, using all of the SST electron channels with the method described below, when THD was between radial

distances of 6.6 and 9 R_E on the outbound portion of its orbit. When using the single-detector channels (i.e., SST electron channels 1–8), PSDs are only calculated beyond GEO to ensure that they are not adversely biased by shield-penetrating electrons or cross-contamination. Here, we show the results from 19–20 Feb. 2010 between 23:45 and 02:36 UT. The orbit for this period is also shown in Figures 1a and 1b with the period of interest indicated in red. This period is at the end of the recovery phase of a small geomagnetic storm ($Dst_{min} > -60$ nT on 15 Feb.), which included several large substorms. Figures 1c and 1d show the FGM magnetic field and SST electron differential fluxes observed by THD as it traverses the outer radiation belt during this period; these are the data required for calculating electron PSD as a function of μ and K. Note that there are no significant field fluctuations or particle injections observed by THD in this calm, steady period.

3. Methodology and Error Analysis

[8] To calculate relativistic electron PSD, we employ a method based on those of *Chen et al.* [2005] and *Turner and Li* [2008]. First, electron differential fluxes, j, are fit to a power law in energy, E, at each observation time:

$$j(E) = AE^{\gamma}\left[\frac{\#}{cm^2 \cdot s \cdot sr \cdot keV}\right] \quad (1)$$

where A and γ are fitting parameters, differential flux is in the units shown in brackets, and the equivalent energy for each channel is the square root of the product of the channel's high and low energy bounds. Percent error in flux for this fit (which corresponds directly to percent error in PSD) can be calculated for each energy channel (denoted with the index, i) using:

$$\varepsilon_{j_i} = \frac{\left|j(E_i)_{meas} - j(E_i)_{fit}\right|}{j(E_i)_{meas}} \quad (2)$$

Next, PSD, f, is calculated as a function of energy:

$$f(E) = 3.325 \times 10^{-8} \frac{j(E)}{E(E + 2m_0c^2)}\left[\left(\frac{c}{MeV \cdot cm}\right)^3\right] \quad (3)$$

where $m_0c^2 = 0.511$ MeV is the rest mass of an electron times the speed of light squared and the numeric factor converts to the units shown in brackets when energy units of MeV are used for E. To convert PSD from a function of energy to a function of μ, the local magnetic field is required. THD FGM data (as shown in Figure 1d) is used to calculate the first adiabatic invariant as a function of energy with:

$$\mu(E, B) = \frac{E(E + 2m_0c^2)}{2Bm_0c^2}\left[\frac{Mev}{G}\right] \quad (4)$$

where B is the local magnetic field strength in Gauss, and the resulting units are shown in brackets. With $\mu(E, B)$, one can then find $f(\mu)$ by using $j(E)$ for the appropriate energies that maintain constant μ given variations in the magnetic field strength. Note that we do not extrapolate, so PSD is undefined when the E required for constant μ is outside of the SST energy range.

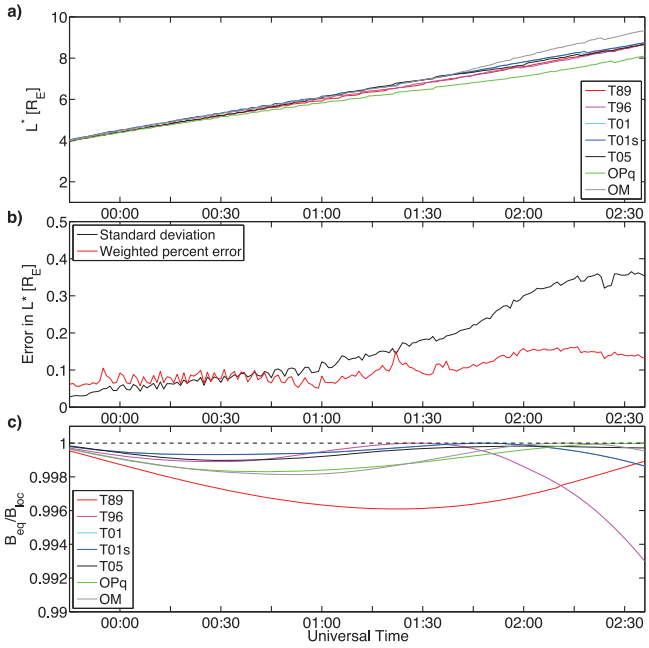

Figure 2. Magnetic field model results and error estimates. (a) L^* as calculated by seven different geomagnetic field models during the period of interest (23:45–02:36 UT on 19–20 Feb. 2010). Results from different models are shown with different colors as indicated on the legend. (b) Estimated error in L^* based on the standard deviation in the models shown in Figure 2a (black curve) and the mean weighted percent error of each model compared to T05 (red curve). The weighted percent error accounts for individual model performance based on the results of *McCollough et al.* [2008]. (c) The ratio of the equatorial field strength (B_{eq}) to the local field strength (B_{loc}) at TH-D calculated for each of the models. This value is used to calculate the error in flux assuming equatorially mirroring particles (i.e., $\alpha_{eq} = 90°$ and $K = 0$ $G^{1/2}R_E$).

[9] To get PSD for fixed second invariant, K, we take advantage of THEMIS orbits being in the magnetic equatorial region. PSD is calculated using only flux for locally mirroring electrons (i.e., local pitch angle, α_{loc}, of 90°). To account for the finite field of view of the SST instruments (FoV ≈ 22°), fluxes are taken from a local pitch angle range spanning 75°–105°. A 3.4% error (from $1.0 - \sin(75°)$, assuming a $\sin^n(\alpha_{eq})$ pitch angle distribution) is included for the flux to account for this ±15° spread in pitch angle. To test the proximity of THD to the magnetic equator and establish uncertainty in the result, we compare results from a series of magnetic field models. Figure 2c shows the ratio between equatorial field strength and local field strength at the THD location during the period of interest on 19–20 Feb. 2010 using seven different field models: five from the Tsyganenko-series of models [*Tsyganenko and Sitnov*, 2005, and references therein], the Olson-Pfitzer quiet model [*Olson and Pfitzer*, 1977], and the *Ostapenko and Maltsev* [1997] model. Input for these models is taken from the *Qin et al.* [2007] appended database of OMNI solar wind quantities at 1 AU and magnetic field model input parameters. Note from Figure 2c that all of the models reveal an equatorial-to-local field strength ratio very close to 1,

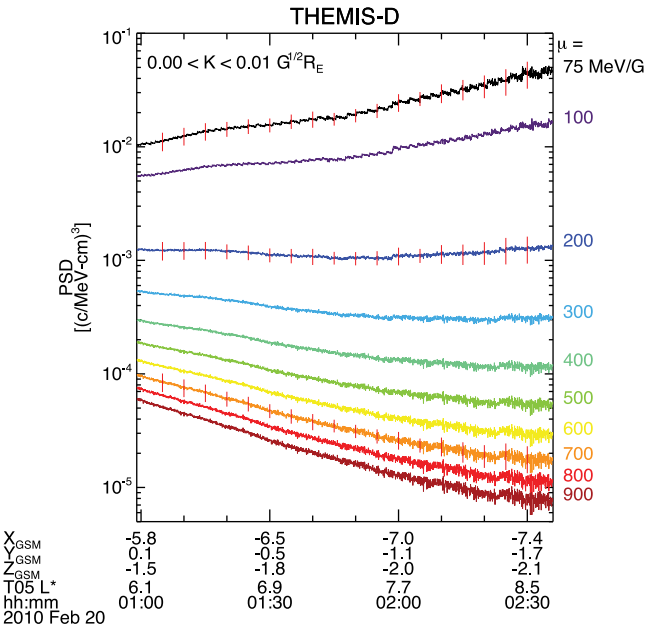

Figure 3. Phase space density derived from the first 11 SST electron channels revealing μ-dependent PSD gradients beyond GEO. The time period shown is 00:59–02:36 UT on 20 Feb. 2010, when TH-D was between radial distances of 6 and 9 R_E. PSD results for different values of the first adiabatic invariant, μ, are shown with different colors, with the corresponding values of μ in MeV/G listed on the right side of the plot. PSD for locally mirroring (α_{loc} = 90°, with the corresponding range in K shown based on the finite field of view of the SST) are shown. For μ = 75, 200, and 700 MeV/G, estimated errors in PSD are shown with the red error bars at five minute intervals.

meaning that TH-D is very near the magnetic equator. Indeed, when $K(\alpha_{loc} = 90°)$ is calculated using these seven models, it reveals that $K = 0.0 \pm 4 \times 10^{-5}$ $G^{1/2}R_E$, accounting for the mean standard deviation in the models' results for the period of interest. Error in PSD resulting from K not being exactly zero can be estimated by assuming a $\sin^n(\alpha_{eq})$ pitch angle distribution and using the conservation of the first adiabatic invariant. Assuming a realistic distribution of n = 1 [*Gannon et al.*, 2007; *Gu et al.*, 2011], percent error in flux (corresponding directly to percent error in PSD) can be calculated as:

$$\varepsilon_K = \frac{j_{eq} - j_{loc}}{j_{eq}} = \frac{j_{eq} - j_{eq}\sin(\alpha_{eq})}{j_{eq}} = 1 - \sin(\alpha_{eq}) = 1 - \sqrt{\frac{B_{eq}}{B_{loc}}} \quad (5)$$

for any off-equatorial flux, j_{loc}, at corresponding equatorial pitch angle, α_{eq}. By conserving the first adiabatic invariant, it is straightforward to show that this error can be expressed in the final form, which is why the ratio of equatorial to local field strengths is shown in Figure 2c. Based on the pitch angle distribution observed here, the $\sin(\alpha_{eq})$ distribution is appropriate, and considering the proximity of THD to the magnetic equator, the resulting error is very small (<1%). In general, a $\sin^n(\alpha_{eq})$ distribution may not always fit, especially considering the effects of drift shell splitting. For such cases where drift shell splitting results in butterfly distributions, either based on observations or L^* estimates, an appropriate pitch angle distribution model should be employed.

[10] To calculate the third adiabatic invariant, L^*, we use the same seven magnetic field models used to calculate K. The results for the period of interest are shown in Figure 2a. Since L^* cannot be determined observationally, these model results are our best estimate for the third invariant. Uncertainty in these results can be estimated using either the standard deviation or a weighted percent difference that takes model performance into account. In Figure 2b, the standard deviation of all the models at each time is shown in black; note that the error increases as L^* increases, which is expected since the model uncertainty is higher in the increasingly stretched or compressed fields further away from the Earth. Also shown in Figure 2b with the red curve is the mean weighted percent difference of each model (denoted with the index, i) from the *Tsyganenko and Sitnov* [2005] (T05) model:

$$\varepsilon_{L^*} = mean\left(\frac{W_i\varepsilon_i}{\sum_i W_i}\right) \quad (6)$$

where the weighting coefficients for each model, W_i, are quantified using model performances from *McCollough et al.* [2008] (quantified using prediction efficiencies for magnetic field strength from each model calculated for GOES-8 for 1996), and the percent difference in L^* of each model, ε_i, with respect to the T05 model (since it is not compared in *McCollough et al.* [2008]) is:

$$\varepsilon_i = \frac{\left|L^*_{T05} - L^*_i\right|}{L^*_{T05}} \quad (7)$$

This is not an exact measure of error, the calculation of which is complicated to define considering that the true L^* cannot be observed directly. However, it is a more accurate representation of uncertainty in L^* than standard deviation since it accounts for the differences between model results and the actual performance of each model.

[11] To analyze PSD throughout the entire outer belt, data from the SST coincidence-logic energy channels have been used, since they do not suffer from species cross-contamination. However, in the heart of the outer belt, where there is a significant population of >1 MeV electrons, contamination due to shield-penetrating electrons must also be accounted for. To do this, we use count rates from the highest SST coincidence channel, which responds to those electrons in the energy range of approximately 1–4 MeV. For contamination in each channel, we use efficiencies from Geant4 simulations of shield-penetrating electrons, and a large geometric factor (64× that of the signal) to account for these contaminating particles entering the instrument from a wide range of angles and depositing energy in all three detectors.

4. Results

[12] First, we investigated the PSD gradients for equatorially mirroring electrons beyond GEO over a wide range of μ (i.e., 75–900 MeV/G) calculated using the first 11 energy channels of SST. The results are shown in Figure 3. It is

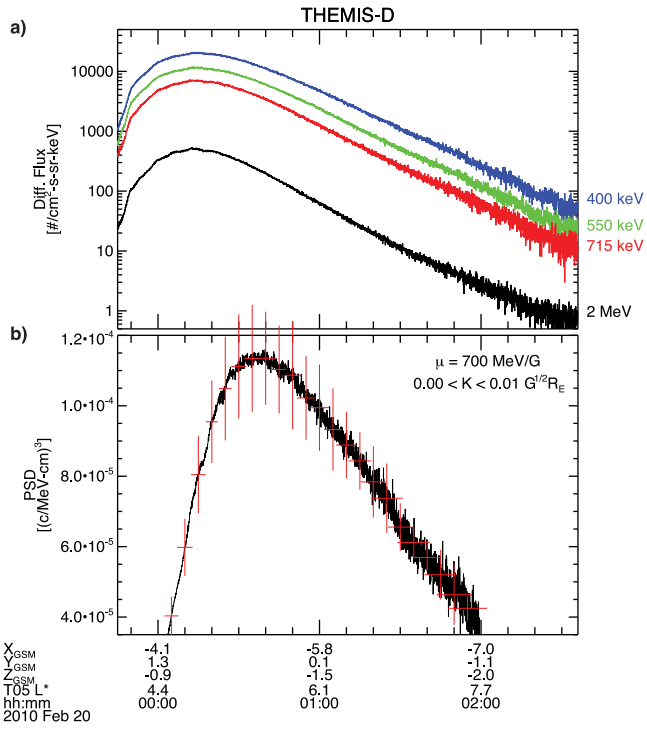

Figure 4. Phase space density derived from the coincidence logic channels throughout the outer radiation belt revealing a peak in PSD at $L^* \approx 5.5$. (a) Electron fluxes from the 2-detectors (blue, green, and red curves) and 3-detectors (black curve) coincident SST channels, with approximate corresponding energies shown on the right of the plot. (b) PSD distribution for $\mu = 700$ MeV/G, locally mirroring ($\alpha_{loc} = 90°$, with the corresponding range in K shown based on the finite field of view of the SST) electrons. Estimated error in PSD (vertical lines) and L^* (horizontal lines) are shown with the red error bars at five minute intervals. Note that the lower limit of the plot (i.e., PSD = 3.5e–5 (c/MeV-cm)^3) corresponds approximately to where μ can no longer be defined at higher L-shells for 700 MeV/G provided the limited energy range of these channels (and thus PSD is no longer defined here).

evident that PSD radial gradients are μ-dependent: they are positive for electrons with $\mu < \sim$200 MeV/G, flat for those with $\mu \approx 200$ MeV/G, and negative for those with $\mu > \sim$200 MeV/G. Around 200 MeV/G is a transition point; the gradients are increasingly positive (negative) for decreasing (increasing) values of μ. Error bars for PSD, which are calculated based on the error in fitting, pitch angle range, and K as discussed above, are also shown for $\mu = 75$, 200, and 700 MeV/G. These results clearly show that the derived distributions are truly present in the observations since the errors are small and do not change the sign of the gradient. With these results, the PSD gradients (df/dL^*) can be quantified. The gradients are $+1.0 \times 10^{-2}$, 0.0×10^{-3}, and -3.6×10^{-5} (c/MeV-cm)^3/R$_E$ for $\mu = 75$, 200, and 700 MeV/G, respectively. These results are entirely consistent with those of *Turner and Li* [2008] and *Kim et al.* [2010], yet they are derived from an entirely independent, equatorial dataset (i.e., THEMIS-SST) and allow for accurate quantification of the radial gradients of PSD and uncertainties associated with data fitting and the use of magnetic field models.

[13] Next, we investigated the PSD of the relativistic population of electrons across the entirety of the outer radiation belt using the SSTs' coincidence channels, which are unaffected by species cross-contamination and corrected for background electrons. An example of the results is shown in Figure 4 for $\mu = 700$ MeV/G and $K = 0.000$ G$^{1/2}$R$_E$. In Figure 4a, the differential fluxes from the four coincidence-logic energy channels are shown, with their approximate equivalent energies listed on the right. Note that the outer belt is clearly resolved: at the start of the period, THD is entering the outer belt from the slot region, encountering the peak in fluxes at $L^* \approx 4.8$. After the peak, the fluxes drop slowly as THD moves to higher L^*. For the PSD results derived from these fluxes (shown in Figure 4b), we tested sensitivity to reasonable variation in the assumptions made to decontaminate the data. The results are consistent for all variations: the PSD distribution in L^* for relativistic electrons through the outer radiation belt is peaked with a maximum at $L^* \approx 5.5$. The peak is significant considering the error bars for PSD and the uncertainty estimates in L^*, which are shown with red bars for every five minutes on Figure 4b. These peaked distributions are also revealed for the range of μ that it was possible to investigate using only the coincidence channels, i.e., $\mu = 500$–2500 MeV/G. These results are also consistent with those of *Selesnick and Blake* [2000], *Green and Kivelson* [2004], *Chen et al.* [2007], and *Shprits et al.* [2007]. However, these results are derived from an entirely independent dataset, and unlike those previous studies, this peaked PSD distribution is shown for equatorially mirroring electrons, so any ambiguity due to changes in the pitch angle distribution is avoided.

[14] Finally, when results from the full period (i.e., 01 Feb.–31 Mar. 2010) were examined, we found that the μ-dependent gradients beyond GEO and peaked relativistic distributions in L^* are typical for the outer radiation belt electrons. Of the 59 days examined, 46 days revealed μ-dependent gradients beyond GEO, all of which were with positive or flat gradients for $\mu < 200$ MeV/G but flat or negative for $\mu > 200$ MeV/G. Of the remaining days, there were 2 days in which the gradients for the full range examined were positive, 1 day in which they were all negative, and 10 days where the gradients were unclear due to either too much activity or saturated SST detectors. For the relativistic population, 28 days revealed clear peaks in the PSD distribution in L^*, with 14 days revealing no clear peak, and unresolved results for the remaining 17 days.

[15] To interpret the results from 19–20 Feb., it is important to note that L^* is defined for the whole period based on all of the models used. So, the peak in PSD is not a result of THD crossing the trapping boundary, which is consistent with the continuity of the flux observations beyond GEO. Interestingly, the days leading up to 20 Feb., during the recovery phase of the storm, also reveal μ-dependent gradients and peaked PSD distributions. However, due to activity during the main phase and instrument saturation during the most intense part of the recovery phase, a clear (i.e., above the error bars) increase in the peak of PSD was not observable. Several mechanisms can result in a peak in PSD, including internal acceleration, losses at higher L^*, and an on-off source at higher L^*.

[16] The μ-dependent gradients and peaked relativistic PSD distributions that we observed are most consistent with the theory of local acceleration by wave-particle interactions. According to theory, plasma sheet particles introduced into the inner magnetosphere via enhanced convection and/or substorm injections serve as a source population for various waves and the seed population required to be accelerated to relativistic energies by those same waves (i.e., whistler-mode chorus [e.g., *Summers et al.*, 1998] and fast magnetosonic waves [e.g., *Horne et al.*, 2007]). Additionally, *Horne et al.* [2005] discussed a critical energy at ~500 keV (corresponding to $\mu \approx 200$ MeV/G at the heart of the outer belt) below which chorus tends to scatter electrons causing loss and above which chorus tends to accelerate electrons. Thus, above this cutoff, electrons should develop a peak in their PSD distributions in their source region, where acceleration is occurring; below this cutoff, electrons should have PSD distributions with a positive gradient, since their source lies in the plasma sheet. We can rule out loss at higher L^* as a mechanism since this would result in negative gradients beyond GEO independent of μ. We cannot entirely rule out the on-off source mechanism though. During some of the most active times, we found mostly flat distributions of relativistic electrons beyond GEO, which is consistent with the results from SCATHA observations of a storm on 02 May 1986 studied by *Fennell and Roeder* [2008]. Thus, a time dependent source at high L^* may still play a role at times. However, considering the strong evidence in support of local acceleration, an alternate interpretation is that enhanced diffusion during active times may smooth the peaked distribution at higher L-shells (since the diffusion coefficient is much higher at higher L^*), essentially balancing any ongoing, enhanced source in the heart of the belt. This mechanism could serve as a limiting factor on the magnitude of the outer belt relativistic population. Ultimately, THEMIS is necessary to help disambiguate scenarios like this during the RBSP era, since it can routinely provide the required observations of PSD beyond the RBSP apogee.

5. Conclusions

[17] Here, we have investigated the PSD distributions in L^* for equatorially mirroring ($K = 0$ $G^{1/2}R_E$) outer belt electrons over a broad range of μ from 75 to 2500 MeV/G. We have three main conclusions:

[18] 1. We have developed a method for estimating error and uncertainty in $f(\mu, K, L^*)$, which allows us to examine significant features in electron PSD distributions. This method should prove useful for future PSD analysis during the upcoming RBSP era and is required for data assimilation.

[19] 2. We have quantified PSD gradients beyond GEO for the first time with equatorially mirroring electrons, and they are most often μ-dependent: they are consistently positive for electrons with $\mu <$ ~200 MeV/G and negative for those with $\mu >$ ~200 MeV/G.

[20] 3. The PSD distribution in L^* throughout the outer radiation belt is most often peaked for the first time with equatorially mirroring, relativistic electrons. The peak is observed at $L^* \approx 5.5$.

[21] These results stem from the recent improvements made in calibrating and characterizing the THEMIS-SST data. These results are consistent with previous studies and agree well with the theory of wave-particle interactions in accelerating a seed population of electrons to relativistic energies in the heart of the belt, yet they are from an entirely independent dataset and are the first to include error bars and to provide such observations from the magnetic equator. Further study is required to disambiguate the cause of peaks in relativistic electron PSD not directly related to loss at higher L^*. In particular, we must determine if these peaks develop from a source in the heart of the outer belt or a time-dependent source at higher L^* or some combination of the two. Since THEMIS can provide PSD observations of the source, seed, and relativistic populations from beyond the RBSP apogee (inside of GEO), up to the magnetopause on the dayside, and into the plasma sheet on the nightside, it will prove invaluable during the RBSP-era for resolving these questions and more concerning outer belt electron sources, losses, and transport.

[22] **Acknowledgments.** We would like to thank the THEMIS mission and instrument teams; Victor Kai for assistance with Geant4 simulations; Janet Green for useful discussions on estimating error in PSD; the Geant4 (http://geant4.cern.ch/) development team; and the development teams for the IRBEM library (http://craterre.onecert.fr/prbem/irbem/description.html) and SpacePy tools (http://spacepy.lanl.gov/). This work was funded under NASA contract NAS5-02099.

[23] The Editor thanks James McCollough and Reiner Friedel for assisting with the evaluation of this paper.

References

Angelopoulos, V. (2008), The THEMIS mission, *Space Sci. Rev.*, *141*, 5–34, doi:10.1007/s11214-008-9336-1.

Auster, H. U., et al. (2008), The THEMIS fluxgate magnetometer, *Space Sci. Rev.*, *141*, 235–264, doi:10.1007/s11214-008-9365-9.

Chen, Y., R. H. W. Friedel, G. D. Reeves, T. G. Onsager, and M. F. Thomsen (2005), Multisatellite determination of the relativistic electron phase space density at geosynchronous orbit: Methodology and results during geomagnetically quiet times, *J. Geophys. Res.*, *110*, A10210, doi:10.1029/2004JA010895.

Chen, Y., et al. (2007), The energization of relativistic electrons in the outer Van Allen radiation belt, *Nat. Phys.*, *3*, 614–617, doi:10.1038/nphys655.

Fennell, J. F., and J. L. Roeder (2008), Storm time phase space density radial profiles of energetic electrons for small and large K values: SCATHA results, *J. Atmos. Sol. Terr. Phys.*, *70*, 1760–1773, doi:10.1016/j.jastp.2008.03.014.

Gannon, J. L., X. Li, and D. Heynderickx (2007), Pitch angle distribution analysis of radiation belt electrons based on Combined Release and Radiation Effects Satellite Medium Electrons A data, *J. Geophys. Res.*, *112*, A05212, doi:10.1029/2005JA011565.

Green, J. C., and M. G. Kivelson (2004), Relativistic electrons in the outer radiation belt: Differentiating between acceleration mechanisms, *J. Geophys. Res.*, *109*, A03213, doi:10.1029/2003JA010153.

Gu, X., Z. Zhao, B. Ni, Y. Shprits, and C. Zhou (2011), Statistical analysis of pitch angle distribution of radiation belt energetic electrons near the geostationary orbit: CRRES observations, *J. Geophys. Res.*, *116*, A01208, doi:10.1029/2010JA016052.

Horne, R. B., R. M. Thorne, S. A. Glauert, J. M. Albert, N. P. Meredith, and R. R. Anderson (2005), Timescale for radiation belt electron acceleration by whistler mode chorus waves, *J. Geophys. Res.*, *110*, A03225, doi:10.1029/2004JA010811.

Horne, R. B., R. M. Thorne, S. A. Glauert, N. P. Meredith, D. Pokhotelov, and O. Santolík (2007), Electron acceleration in the Van Allen radiation belts by fast magnetosonic waves, *Geophys. Res. Lett.*, *34*, L17107, doi:10.1029/2007GL030267.

Kim, H.-J., E. Zesta, K.-C. Kim, Y. Shprits, Y. Shi, and L. R. Lyons (2010), Estimation of radial gradients of phase space density from POLAR observations during a quiet period prior to a sudden solar wind dynamic pressure enhancement, *J. Geophys. Res.*, *115*, A12249, doi:10.1029/2010JA015722.

McCollough, J. P., J. L. Gannon, D. N. Baker, and M. Gehmeyr (2008), A statistical comparison of commonly used external magnetic field models, *Space Weather*, *6*, S10001, doi:10.1029/2008SW000391.

McFadden, J. P., et al. (2008), The THEMIS ESA plasma instrument and in-flight calibration, *Space Sci. Rev.*, *141*, 277–302, doi:10.1007/s11214-008-9440-2.

Olson, W. P., and K. A. Pfitzer (1977), Magnetospheric magnetic field modeling, Annual Scientific Report, AFOSR contract F44620-75-C-0033, McDonnell Douglas Astronaut. Co., Huntington Beach, Calif.

Ostapenko, A. A., and Y. P. Maltsev (1997), Relation of the magnetic field in the magnetosphere to the geomagnetic and solar wind activity, *J. Geophys. Res.*, *102*(A8), 17,467–17,473, doi:10.1029/97JA00937.

Qin, Z., R. E. Denton, N. A. Tsyganenko, and S. Wolf (2007), Solar wind parameters for magnetospheric magnetic field modeling, *Space Weather*, *5*, S11003, doi:10.1029/2006SW000296.

Selesnick, R. S., and J. B. Blake (2000), On the source location of radiation belt relativistic electrons, *J. Geophys. Res.*, *105*(A2), 2607–2624, doi:10.1029/1999JA900445.

Shprits, Y., D. Kondrashov, Y. Chen, R. Thorne, M. Ghil, R. Friedel, and G. Reeves (2007), Reanalysis of relativistic radiation belt electron fluxes using CRRES satellite data, a radial diffusion model, and a Kalman filter, *J. Geophys. Res.*, *112*, A12216, doi:10.1029/2007JA012579.

Summers, D., R. M. Thorne, and F. Xiao (1998), Relativistic theory of wave-particle resonant diffusion with application to electron acceleration in the magnetosphere, *J. Geophys. Res.*, *103*(A9), 20,487–20,500, doi:10.1029/98JA01740.

Tsyganenko, N. A., and M. I. Sitnov (2005), Modeling the dynamics of the inner magnetosphere during strong geomagnetic storms, *J. Geophys. Res.*, *110*, A03208, doi:10.1029/2004JA010798.

Turner, D. L., and X. Li (2008), Radial gradients of phase space density of the outer radiation belt electrons prior to sudden solar wind pressure enhancements, *Geophys. Res. Lett.*, *35*, L18101, doi:10.1029/2008GL034866.

Turner, D. L., X. Li, G. D. Reeves, and H. J. Singer (2010), On phase space density radial gradients of Earth's outer-belt electrons prior to sudden solar wind pressure enhancements: Results from distinctive events and a superposed epoch analysis, *J. Geophys. Res.*, *115*, A01205, doi:10.1029/2009JA014423.